Loughborough University

This item was submitted to Loughborough's Research Repository by the author.
Items in Figshare are protected by copyright, with all rights reserved, unless otherwise indicated.

Hysteretic sediment fluxes in rainfall-driven soil erosion: particle size effects

PLEASE CITE THE PUBLISHED VERSION

http://dx.doi.org/10.1002/2016WR019314

PUBLISHER

© American Geophysical Union (AGU)

VERSION

VoR (Version of Record)

PUBLISHER STATEMENT

This work is made available according to the conditions of the Creative Commons Attribution-NonCommercial-NoDerivatives 4.0 International (CC BY-NC-ND 4.0) licence. Full details of this licence are available at: https://creativecommons.org/licenses/by-nc-nd/4.0/

LICENCE

CC BY-NC-ND 4.0

REPOSITORY RECORD

Cheraghi, Mohsen, Seifeddine Jomaa, Graham Sander, and D. Andrew Barry. 2016. “Hysteretic Sediment Fluxes in Rainfall-driven Soil Erosion: Particle Size Effects”. Loughborough University. https://hdl.handle.net/2134/23143.

AGU PUBLICATIONS

Water Resources Research

RESEARCH ARTICLE
10.1002/2016WR019314

Hysteretic sediment fluxes in rainfall-driven soil erosion: Particle size effects

Mohsen Cheraghi[1], Seifeddine Jomaa[2], Graham C. Sander[3], and D. A. Barry[1]

[1]Laboratoire de technologie écologique, Institut d'ingénierie de l'environnement, Faculté de l'environnement naturel, architectural et construit (ENAC), Ecole Polytechnique Fédérale de Lausanne (EPFL), Lausanne, Switzerland, [2]Department of Aquatic Ecosystem Analysis and Management, Helmholtz Centre for Environmental Research—UFZ, Magdeburg, Germany, [3]Department of Civil and Building Engineering, Loughborough University, Loughborough, United Kingdom

Key Points:
- Hysteresis is attenuated with increasing sediment size
- The Hairsine and Rose soil erosion model reproduce hysteresis patterns
- Hysteresis is a manifestation of the changing composition of the surface layer

Correspondence to:
M. Cheraghi,
mohsen.cheraghi@epfl.ch

Citation:
Cheraghi, M., S. Jomaa, G. C. Sander, and D. A. Barry (2016), Hysteretic sediment fluxes in rainfall-driven soil erosion: Particle size effects, *Water Resour. Res.*, *52*, 8613–8629, doi:10.1002/2016WR019314.

Received 6 JUN 2016
Accepted 23 OCT 2016
Accepted article online 1 NOV 2016
Published online 12 NOV 2016

© 2016. American Geophysical Union. All Rights Reserved.

Abstract A detailed laboratory study was conducted to examine the effects of particle size on hysteretic sediment transport under time-varying rainfall. A rainfall pattern composed of seven sequential stepwise varying rainfall intensities (30, 37.5, 45, 60, 45, 37.5, and 30 mm h^{-1}), each of 20 min duration, was applied to a 5 m × 2 m soil erosion flume. The soil in the flume was initially dried, ploughed to a depth of 20 cm and had a mechanically smoothed surface. Flow rates and sediment concentration data for seven particle size classes (<2, 2–20, 20–50, 50–100, 100–315, 315–1000, and >1000 μm) were measured in the flume effluent. Clockwise hysteresis loops in the sediment concentration versus discharge curves were measured for the total eroded soil and the finer particle sizes (<2, 2–20, and 20–50 μm). However, for particle sizes greater than 50 μm, hysteresis effects decreased and suspended concentrations tended to vary linearly with discharge. The Hairsine and Rose (HR) soil erosion model agreed well with the experimental data for the total eroded soil and for the finer particle size classes (up to 50 μm). For the larger particle size classes, the model provided reasonable qualitative agreement with the measurements although the fit was poor for the largest size class (>1000 μm). Overall, it is found that hysteresis varies amongst particle sizes and that the predictions of the HR model are consistent with hysteretic behavior of different sediment size classes.

1. Introduction

Estimates of temporal variations of suspended load with discharge are needed for the assessment of aquatic ecosystems, estimates of contaminant export from catchments, and the prediction of stream water quality [*Walling and Webb*, 1985; *Wood and Armitage*, 1997; *Batalla et al*., 2004; *O'Connell and Siafarikas*, 2010; *Rossi et al*., 2013; *Halliday et al*., 2014; *Karimaee Tabarestani and Zarrati*, 2014; *Lloyd et al*., 2016]. The relationship between discharge and sediment concentration is available for different catchments and rivers [*Klein*, 1984; *Williams*, 1989; *Seeger et al*., 2004; *Nadal-Romero et al*., 2008; *Sadeghi et al*., 2008; *Smith and Dragovich*, 2009; *Eder et al*., 2010; *Alemayehu et al*., 2014; *De Girolamo et al*., 2015; *Sun et al*., 2016; *Dean et al*., 2016; *Sheriff et al*., 2016]. Depending on the variation of discharge and sediment concentration versus time, different hysteretic concentration-discharge curves can be generated including clockwise, anticlockwise, and figure eight. At the plot scale, *Strohmeier et al*. [2016] examined soil erosion under temporally variable rainfall at two different locations and assessed the effect of extreme rainfall events on long-time erosion. They reported that a few extreme rainfall events can have a permanent effect on land degradation in contrast to lower intensity but frequent events. Their results also show the opposite case, i.e., that the soil loss can be mainly caused by a large number of low intensity rainfall events rather than the rainfall extremes. The different patterns were due to spatially variable factors in the landscape such as soil type, land use, and slope.

Hysteresis loops are a feature of plot-scale and catchment-scale sediment transport. Several studies investigated the factors and processes responsible for these loops in order to interpret or determine the distribution of sediment sources within a catchment [*Seeger et al*., 2004; *Smith and Dragovich*, 2009; *Yeshaneh et al*., 2014]. The difficulty of interpretation at these scales is that there are complications arising from spatial and temporal variability in climate [*Ghahramani and Ishikawa*, 2013; *Arjmand Sajjadi and Mahmoodabadi*, 2015; *Dai et al*., 2016], soil types [*Keesstra et al*., 2014; *Rodrigo Comino et al*., 2016], land use [*Cerdà et al*., 2009; *Prosdocimi et al*., 2016], topography [*Ghahramani et al*., 2012], catchment connectivity [*Ghahramani and Ishikawa*, 2013; *Marchamalo et al*., 2015; *Masselink et al*., 2016], channel storage and bank erosion [*Buendia*

et al., 2015], and soil saturation and the initial condition of the surface soil [*Seeger et al*., 2004; *Bussi et al*., 2014; *Kim and Ivanov*, 2014; *Pietroń et al*., 2015]. Hysteresis patterns are generally seen as complex and their interpretation is not straightforward [*Gao and Josefson*, 2012; *Aich et al*., 2014].

Simplified laboratory systems are more amenable to develop understanding of specific processes. For instance, hysteresis loops can be obtained under a single-peak individual storm event on a planar landscape. For this case, *Sander et al*. [2011] conducted simulations using the Hairsine and Rose (HR) model [*Hairsine and Rose*, 1991, 1992] in which variations in the initial condition of the deposited layer (i.e., previously eroded soil) were imposed. They found that not only were all the specific forms of the hysteretic loops of *Williams* [1989] (i.e., clockwise—using a well-developed spatially uniform deposited layer at t (time) = 0, counter-clockwise—using no deposited layer at $t = 0$, and figure eight—having a spatially varying deposited layer at $t = 0$) straightforward to reproduce, but they could also replicate the same patterns found in catchment studies by *Eder et al*. [2010] and *Oeurng et al*. [2011]. Subsequently, *Zhong* [2013] extended the results of *Sander et al*. [2011] to demonstrate that a variety of multilooped hysteresis patterns could be obtained without the need for flows over a complex topography or for multiple storm events.

The work of *Sander et al*. [2011] and *Zhong* [2013] shows that the HR model reproduces hysteretic loops in sediment concentration versus discharge as a result of two factors. First, the model accounts for the spatial variability in the distribution of easily erodible sediment at the start of an event. Second, it accounts for deposition as a separate rate process and as such directly models the preferential deposition of different sediment sizes resulting in the growth of a deposited layer having different erosive characteristics to the original soil bed. Thus, hysteresis is a result of interactions between the time-varying overland flow and differences between the cohesive strength of the original uneroded soil and deposited layer. Consequently "the [initial] spatial distribution and particle size composition of previously deposited sediment plays a significant role in determining the erosive response of the land surface" [*Sander et al*., 2011].

The role of the surface soil composition and soil compaction due to rainfall was investigated by *Jomaa et al*. [2013], who reported experimental data and associated modeling (using the HR model) of rainfall-driven erosion. They applied multiple rainfall events separated by a drying period, which enabled them to investigate the effect of initial soil conditions (surface sealing, wetting-drying cycles, and initial moisture content). They found that "the soil erosion short-time response is mainly controlled by the initial conditions, whereas the long-time behavior is controlled by the precipitation rate only." Following this work, the importance of initial surface sediment conditions was considered by *Bussi et al*. [2014], who modeled sediment transport of the Goodwin Creek catchment. They found that the "estimation of the loose deposited sediments at the beginning of the storm event is fundamental for proper event scale modeling of soil erosion and sediment transport of the Goodwin Creek catchment." *Bussi et al*. [2014] simulated the different hysteresis loops of *Williams* [1989], although they had mixed success in reproducing the correct orientation and loop size of the experimental data.

In more recent work on the role of initial conditions in soil erosion, *Kim and Ivanov* [2014] and *Kim et al*. [2016a, 2016b] have recently further developed and confirmed the findings of *Sander et al*. [2011] and *Jomaa et al*. [2013] by carrying out a series of detailed numerical studies on the effect of the initial deposited layer in the HR model on erosion rates and transport of eroded sediment. *Kim and Ivanov* [2014] considered combinations of two consecutive 1 h storms of differing but constant intensities that were also separated by different time intervals. For combinations were the second storm had the same intensity, quite different sediment transport responses during the second storm were seen, as observed earlier by *Jomaa et al*. [2013]. They also found that this nonuniqueness in the erosive response was due to the first storm resulting in different compositions of the deposited layer (or initial conditions) prior to the start of the second storm. *Kim et al*. [2016b] also demonstrated the role of the subsurface initial moisture content in causing nonunique sediment transport under the same rainfall history. Numerical simulations reported by *Kim et al*. [2016a] on total sediment loss at the plot scale provide evidence (their supporting information Figure S2) of the dependence of clockwise and counter-clockwise hysteresis loops on the initial state of the deposited layer.

Previous studies at the field scale reported hysteresis loops for the total suspended concentration, but not the corresponding results for the different particle size classes [e.g., *Alemayehu et al*., 2014; *De Girolamo et al*., 2015; *Sun et al*., 2016; *Dean et al*., 2016; *Sherriff et al*., 2016]. It is unknown whether all size classes have

the same or different hysteretic behavior as the total concentration. At the laboratory scale, *Polyakov and Nearing* [2003] analyzed flow-driven erosion experiments in which they considered both steady state and time-dependent hysteretic conditions. The steady state experiments were carried out on an 8 m flume for two different inflow boundary conditions, either a zero or constant sediment flux, the latter being greater than the transport capacity of the flow. The volumetric water discharge for both boundary conditions was the same. The transient experiments were performed on a 2 m flume for which the incoming sediment flux at the boundary was cycled every 0.25 h between the two fluxes used in the steady state experiment. Both sets of experiments displayed hysteresis in the total sediment concentration. Hysteresis in the suspended sediment concentrations for the individual size classes was also shown for the steady state experiment; however, size class data were not measured for the transient experiments. *Sander et al*. [2007] subsequently used the HR model to reproduce the steady state results of *Polyakov and Nearing* [2003] for both the total sediment concentration and for the different size classes. For the transient experiments, flow through the flume was supercritical and the bed morphology evolution was coupled with the overland flow. To account for this, *Sander et al*. [2011] extended the finite volume scheme of *Heng et al*. [2009, 2011], which combined the HR model with the Saint-Venant equations for flow and the Exner equation for modeling bed elevation changes. Figure 3 of *Sander et al*. [2011] shows that their model reproduces the rapid rise and fall in total sediment concentration at the end of the flume that results from the periodic sediment flux boundary condition along with the associated hysteretic behavior of the transported sediment.

There appears to be only one time-dependent laboratory study on hysteresis effects in overland flow sediment transport [*Polyakov and Nearing*, 2003], and it considers only the total suspended sediment concentration. There have been no experiments that specifically investigate the role of particle size in hysteretic transport other than the steady state data of *Polyakov and Nearing* [2003]. Consequently, the aim of this paper is to investigate hysteretic sediment transport under rainfall-driven erosion conditions using a well-controlled flume-scale experiment. The experiment involves a symmetric, single-peak rainfall event made up of seven sequential 20 min periods of differing constant intensities, with the peak intensity occurring for the fourth period. Throughout these seven periods, discharge and sediment size class data are measured at the flume outflow in order to quantify hysteresis in particle size class concentrations. The data are analyzed using the HR model, which is shown to reproduce the size class hysteretic behavior displayed by the experimental data. This investigation therefore compliments those of *Sander et al*. [2007, 2011] on flow-driven erosion to the case of rainfall-driven erosion.

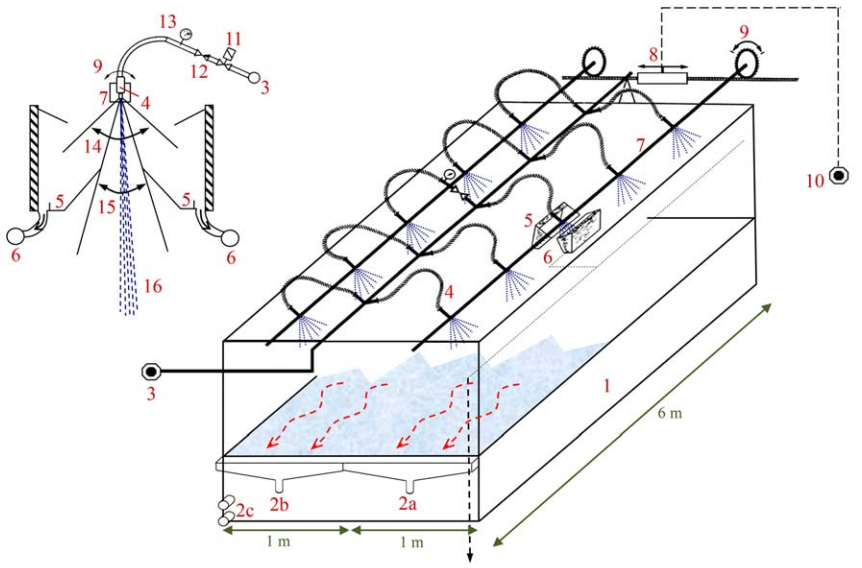
2. Methods

2.1. Experimental Setup

The study was carried out using the 6 m $\times$ 2 m EPFL soil erosion flume with two collectors at the outlet. Rainfall was applied to the lower 5 m of the flume's length from 10 oscillating valves that generate approximately uniform rainfall with a uniformity coefficient of 0.86 [*Tromp-van Meerveld et al*., 2008; *Jomaa et al*., 2010]. The precipitation rate is changed by varying the oscillation frequency of the sprinklers.

Different parts of the flume are shown in Figure 1. More detailed descriptions of the flume characteristics are reported elsewhere [*Viani*, 1986; *Baril*, 1991; *Jomaa et al*., 2010]. The flume was filled with an agricultural loamy soil with 4% clay, 29% silt, 41% sand, and 26% fine gravel from a field near Sullens in the Canton of Vaud, Switzerland. Soil characteristics are given by *Baril* [1991]. After ploughing and disaggregating the topsoil to a depth of 20 cm, a mechanical smoother was moved along the flume several times to ensure a uniform initial surface condition.

For loamy soils, the critical stream power above which entrainment occurs is in the range 0.15–0.20 W m^{-2} [*Beuselinck et al*., 2002]. In this work, the maximum stream power was estimated to be 0.013 W m^{-2} and therefore raindrop-driven erosion was the dominant mechanism of sediment transport. No rills were observed during a visual postexperiment inspection. As seen in Figure 2, the 140 min precipitation period involved symmetric rising and falling limbs, divided into seven consecutive 20 min intervals, which are referred to as rainfall events and are denoted by E1 to E7, respectively. The rainfall intensity increased from 30 mm h^{-1} (E1) up to 60 mm h^{-1} (E4) on the rising limb. During the experiment, flume discharge was collected regularly in half-liter containers (Collectors 1 and 2, Figure 1). Because of higher erosion rate at the beginning of the experiment, sampling was performed continuously for the first 10 min and thereafter



1. Erosion flume
2. Flow collection troughs
   a. Collector 1
   b. Collector 2
   c. Subsurface flow
3. Lake water supply
4. Water outlet tube
5. Collection troughs
6. To storm water drain
7. Rotating bar
8. Oscillator
9. Direction of oscillation
10. Compressor
11. Magnetic vane
12. Regulator
13. Manometer
14. Maximum oscillation amplitude (90°)
15. Actual water outlet (30°)
16. Water jet

Figure 1. Schematic of the EPFL soil erosion flume. The flume slope can be varied between 0% and 30%. Precipitation is applied using 10 oscillating sprinklers located 3 m above the soil surface.

every 3 min. The size and proportion of the particle size classes are presented in Table 1. The collected samples were used to determine discharge rates and sediment concentrations of the total and individual size classes. Seven size classes were considered (Table 1), with concentrations denoted by C_1–C_7. For sediment

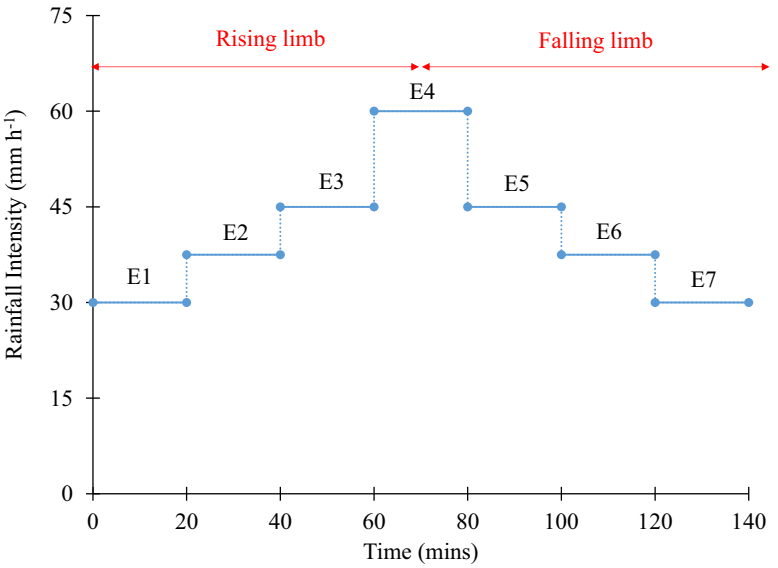


Figure 2. Seven sequential rainfall events, each 20 min long.

Table 1. Properties of Seven Different Particle Size Classes of the Soil[a]

Size Class	Diameter (μm) From	Diameter (μm) To	Proportion (by Mass) in the Original Soil, p_i (%)	Settling Velocity, v_i (m s^{-1}) From	Settling Velocity, v_i (m s^{-1}) To	v_i (m s^{-1}) Used in HR Model
C_1	0	2	3.7	8.0×10^{-8}	4.0×10^{-6}	5.0×10^{-7}
C_2	2	20	19.4	4.0×10^{-6}	4.0×10^{-4}	1.5×10^{-5}
C_3	20	50	8.3	4.0×10^{-4}	2.5×10^{-3}	7.0×10^{-4}
C_4	50	100	8.7	2.5×10^{-3}	1.4×10^{-2}	4.0×10^{-3}
C_5	100	315	17.7	1.4×10^{-2}	3.7×10^{-2}	4.0×10^{-3}
C_6	315	1000	20.6	3.7×10^{-2}	6.9×10^{-2}	4.0×10^{-3}
C_7	>1000		21.6	6.9×10^{-2}	1.4×10^{-1}	6.0×10^{-2}

[a]The settling velocities are from *Tromp-van Meerveld et al.* [2008].

concentration measurements from the collected samples, the larger size classes (>100 μm) were sieved, while for the rest a laser particle size analyzer was employed.

2.2. HR Model

The HR soil-erosion model considers different particle size classes and incorporates a mechanistic description of a shield layer development (that is composed of previously eroded material that helps to protect the original soil from further erosion). This model was investigated theoretically [*Sander et al.*, 1996; *Lisle et al.*, 1998; *Hairsine et al.*, 1999; *Parlange et al.*, 1999; *Barry et al.*, 2010; *Kinnell*, 2013] and validated via zero-dimensional [*Heilig et al.*, 2001; *Gao et al.*, 2003] and flume-scale laboratory experiments [e.g., *Jomaa et al.*, 2010, 2012b, 2013], as well as at the small field [*Van Oost et al.*, 2004] and catchment scales [*Kim et al.*, 2013]. Details of the HR model are available elsewhere [*Hairsine and Rose*, 1991, 1992], so only a brief summary is given here. The model's governing equations in the absence of flow-driven processes are

$$\frac{\partial D}{\partial t} + \frac{\partial q}{\partial x} = R, \tag{1}$$

$$\frac{\partial (DC_i)}{\partial t} + \frac{\partial (qC_i)}{\partial x} = ap_iP(1-H) + \frac{m_i}{m_t}a_dPH - v_iC_i, \quad i=1,\ 2,\ \ldots,\ N, \tag{2}$$

$$\frac{\partial m_i}{\partial t} = v_iC_i - \frac{m_i}{m_t}a_dPH, \quad i=1,\ 2,\ \ldots,\ N, \tag{3}$$

where i refers to particle size class, N is the number of size classes, t, x, D, and C_i denote the time (s), downslope distance (m), surface water depth (m), and suspended sediment concentration, respectively (kg m^{-3}), m_i is the deposited sediment mass per unit area (kg m^{-2}), q is the volumetric water flux per unit width (m^2 s^{-1}), R and P are the excess rainfall and rainfall rates (m s^{-1}), respectively, a is the detachability of the original soil (kg m^{-3}), p_i is the mass proportion of the particle size class i in the original soil, a_d is the detachability of the deposited soil (kg m^{-3}), and v_i is the settling velocity (m s^{-1}). The degree of shielding is measured by $H = m_t/m^*$ in which $m_t = \sum m_i$ is the total mass of the deposited layer and m^* is the required mass for a complete shielding of the original soil.

2.3. Model Application and Parameter Estimation

An analytical approximation of the HR model was presented by *Sander et al.* [1996] and validated by different flume-scale and small-scale experiments [*Heilig et al.*, 2001; *Tromp-van Meerveld et al.*, 2008; *Jomaa et al.*, 2012b, 2013]. In their solution, a uniform suspended concentration is assumed within a constant depth of water, and spatial variability is ignored. The same approach was used in this study. With these assumptions and the combination of equations (1) and (2), the model consists of 14 coupled ordinary differential equations for seven particle size classes. These equations were solved for each 20 min rainfall event (E1–E7). Every 20 min, the final values of the sediment concentrations (C_i) and deposited layer masses (m_i) provided the initial conditions for the next rainfall event.

The settling velocity is an important parameter that determines the deposition rate of the individual particles. The ranges of settling velocity for different particle sizes were measured by *Tromp-van Meerveld et al.* [2008] who used the same flume and sediment (Table 1). For the larger particle size classes (C_4–C_7, Table 1), they used a 0.47 m tube filled with water and for the rest of the particles, the settling velocity was

Table 2. Optimized Parameters (a, a_d, m^*, and D) for Each Rainfall Event

		Rainfall Event						
	Parameter	E1	E2	E3	E4	E5	E6	E7
Collector 1	a (mg cm^{-3})	357	23	21	36	20	25	23
	a_d (mg cm^{-3})	435	464	597	715	485	330	320
	m^* (mg cm^{-2})	11.4	23.6	28.0	33.6	38.5	39.6	40.8
	D (mm)	6.1	7.1	8.0	10.5	8.4	8.3	7.9
Collector 2	a (mg cm^{-3})	230	25	33	35	25	22	26
	a_d (mg cm^{-3})	423	436	480	562	312	239	254
	m^* (mg cm^{-2})	12.8	25.1	28.4	37.4	42.9	45.2	45.5
	D (mm)	4.8	5.4	5.7	6.7	6.0	5.6	5.4

calculated using Stokes' law [*Stokes*, 1850]. They also fitted the model to the experiments to find the optimal settling velocities, some of which were different from the measured values for some of the particle sizes. As discussed in detail by *Tromp-van Meerveld et al*. [2008], possible explanations for this are flocculation, selective rainfall detachment, transport mechanisms rather than suspension, turbulence, hindered settling, the effect of infiltration, and measurement errors. The excess rainfall rate ($R = P - f$) was calculated based on the saturated infiltration rate (f) and the precipitation rate (P). In this experiment, the steady infiltration rates (f) for the different rainfall events were 4.82, 4.84, 4.23, 4.93, 4.24, 4.18, and 4.16 mm h^{-1}, respectively, for E1 to E7. Parameters fitted were detachability (a), redetachability (a_d), mass of the shield layer to protect the original soil (m^*), and water-layer depth (D). The calibrated values for the two collectors are presented in Table 2. An automatic calibration procedure was used for each rainfall event to deduce model parameters. The objective function was defined as the mean square error of the difference between model and experiment for the seven particle size classes, which was minimized using particle swarm optimization [*Kennedy*, 2010].

3. Results and Discussion

3.1. Experiment

3.1.1. Discharge

The discharge rates for each collector are shown in Figure 3. In the first rainfall event (E1, Figure 2), most rainfall infiltrated into the soil during the first 10 min. Afterward, the runoff increased up to a constant value as the soil became saturated, after which infiltration into the soil was constant (4.82 mm h^{-1}). In the following rainfall events (E2–E7, Figure 2), runoff rates generally followed rainfall intensities (Figures 2 and 3). The higher discharge from Collector 2 compared to Collector 1 reflects the two-dimensional flow in the flume. Also, the discharge for the falling rainfall limb (E5–E7) is greater than that in the rising limb (E1–E4) for both collectors. This increase in discharge is due to reduced infiltration into the soil, caused by surface sealing and/or compaction of the soil resulting from raindrop impact. Additionally, due to compaction and overland flow, the surface roughness likely reduced over time, which resulted in increased surface flow rates.

3.1.2. Sediment Concentrations

Figures 4 and 5 show the total sediment concentration (C) and the concentrations of individual particle classes (C_1–C_7) for Collectors 1 and 2, respectively. The maximum total sediment concentration (C) occurs in the first rainfall event, in spite of the low precipitation rate in this period (30 mm h^{-1}). During each of the subsequent rainfall events, C declines to a quasisteady equilibrium. The higher sediment concentrations in the first rainfall event (E1, Figure 2) stems from the initial condition—the soil was ploughed and not compacted prior to the experiment, leading to easily erodible soil. Additionally, there is the initial flush of fine material, which dominates the contribution to the early peak, and then the subsequent decline in C as the development of deposited layer reduces access to the finer soil particles [*Sander et al*., 1996]. During rainfall events E2–E4 (rainfall intensities of 37.5, 45, and 60 mm h^{-1}, respectively), C shows a small increase at the beginning of each precipitation event and rapidly reaches a near-constant value. Finally, during the last three rainfall events (E5–E7), due to the decreasing rainfall intensity, C decreases. Observe that C is higher for the same precipitation rate during the rising limb compared to falling limb, i.e., C is lower during E7 than E1, E6 than E2, and E5 than E3. This is likely due to on-going compaction of the soil caused by raindrop impact and development of the shield layer, leading to reduced availability of erodible fine sediment. Both of these

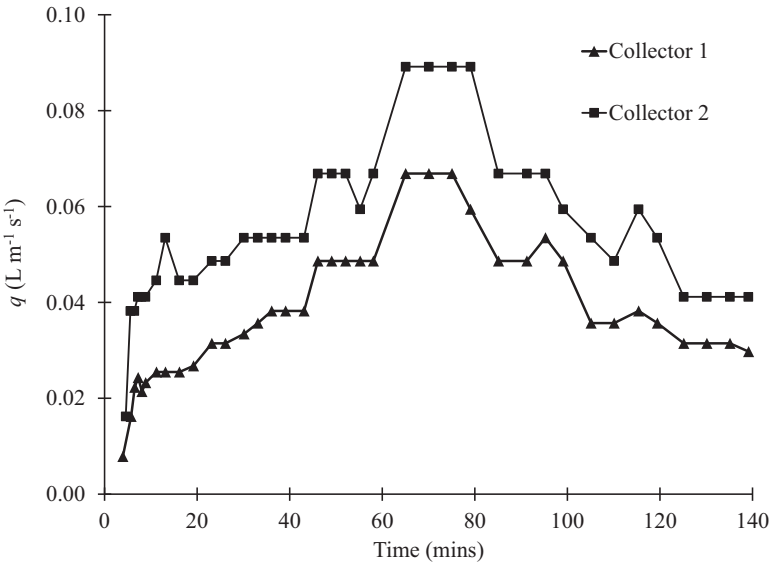


Figure 3. Discharge measured at the two collectors. Except the first rainfall event (precipitation onto a dry soil), the discharge rapidly adapts to changes in rainfall intensity.

effects have been previously observed in flume experiments by *Jomaa et al*. [2012a] and field studies by *Cerdà* [2001], while *Kim and Ivanov* [2014] have also noted the effect of the shield layer development on subsequent rainfall events with their 2-D numerical simulation at the large plot scale. We return to the shield layer below.

The results for the individual particle size classes (Figures 4 and 5) show that their temporal evolutions agree with, or are in contrast to, the overall behavior displayed by C. For instance, the maximum contribution of the two finest size classes (>2 and 2–20 μm, i.e., C_1 and C_2) is at the beginning of the first precipitation period E1, where C_1 reached 1.00 and 1.38 g L^{-1} for Collectors 1 and 2, respectively, with the corresponding values for C_2 being 5.11 and 6.95 g L^{-1}. The calibrated parameters of the HR erosion model (Table 2) for this period also show that the soil detachabilities were greater than for the subsequent rainfall events, where the maximum concentrations decreased regardless of the rainfall intensity (except for a subtle increase occurring for 60 mm h^{-1} during E4). After the second rainfall event, the proportion of the finer particles decreased in the deposited layer (see section 3.1.3) and hence also in the flume discharge. This trend was maintained during the increasing rainfall events of E3 and E4, indicating that the availability of finer sediments decreased over the course of the experiment.

Sediment concentrations were more sensitive to the precipitation rate variation for the middle particle size classes. For particle size C_3, for both collectors (Figures 4 and 5), the concentration at the maximum rainfall intensity (60 mm h^{-1}, E4) was comparable to that of the first rainfall event (30 mm h^{-1}, E1). For particle size class C_4, the two collectors both show that the greatest concentrations appear at the maximum rainfall intensity (60 mm h^{-1}, E4). For Collector 2 (Figure 5), the maximum concentration of C_4 (0.34 g L^{-1}) is at around 5 min, although this point is likely an outlier. The C_4 data from both Collectors 1 and 2 show that if this point were ignored, the same temporal behavior and the same magnitudes for each separate rainfall were measured. Data from Collectors 1 and 2 agree well for all of the size classes as well as total concentration, demonstrating consistent sediment transport on both sides of the flume.

The rainfall intensity had a noticeable impact on the transport of the coarser sediment classes (C_5–C_7). At the precipitation rate of 30 mm h^{-1}, erosion rates of the large particles for the rising limb (E1) tend to be less than for the falling limb (E7), which is opposite to the behavior of the finer particle sizes. Although the condition of the topsoil changes between the second and sixth rainfall events (E2 and E6, 37.5 mm h^{-1}) and the third and fifth rainfall events (E3 and E5, 45 mm h^{-1}), the concentrations of the larger sediment sizes (C_5–C_7) remain approximately equal for the same rainfall intensity on both the rising and falling limbs. In short, the measurements show that the larger particle size concentrations are determined primarily by the precipitation rate, not by the condition of the soil surface. This is likely due to the deposited layer

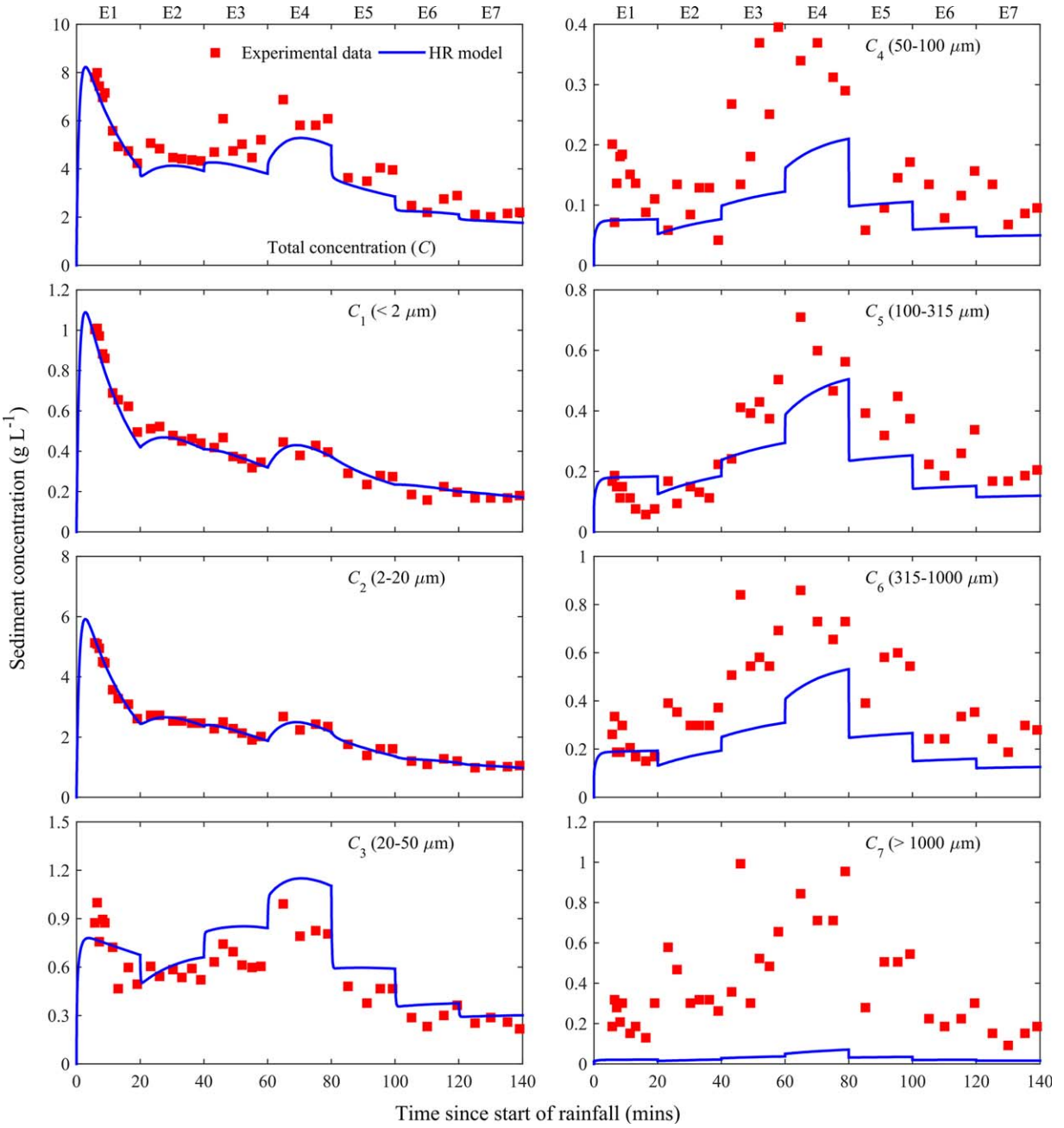


Figure 4. Total sediment concentration (C) and the concentrations of the seven different particle size classes (C_1–C_7) for Collector 1. Regardless of the rainfall intensity, concentrations of the first two size classes decrease with time whereas concentrations of the larger particle sizes vary with the rainfall intensity.

already becoming dominated by the larger particles by the end of E1, thus the soil surface (the deposited layer) undergoes only relatively minor changes during subsequent events [*Sander et al.*, 2011; *Kim and Ivanov*, 2014].

3.1.3. Hysteresis Loops

Figures 6 and 7 show plots of q versus sediment concentration for Collectors 1 and 2, respectively. Although minor differences can be seen, the results for the two collectors are similar. As described above, the maximum total sediment concentration occurs before the maximum discharge (Figures 3–5), thereby generating a clockwise hysteresis loop [*Williams*, 1989; *Sander et al.*, 2011]. As a result of compaction during the early rainfall events, as well as the initial removal of easily erodible fine sediment followed by the greater protection of the soil due to the growth of deposited layer with time, and the subsequent domination of this layer

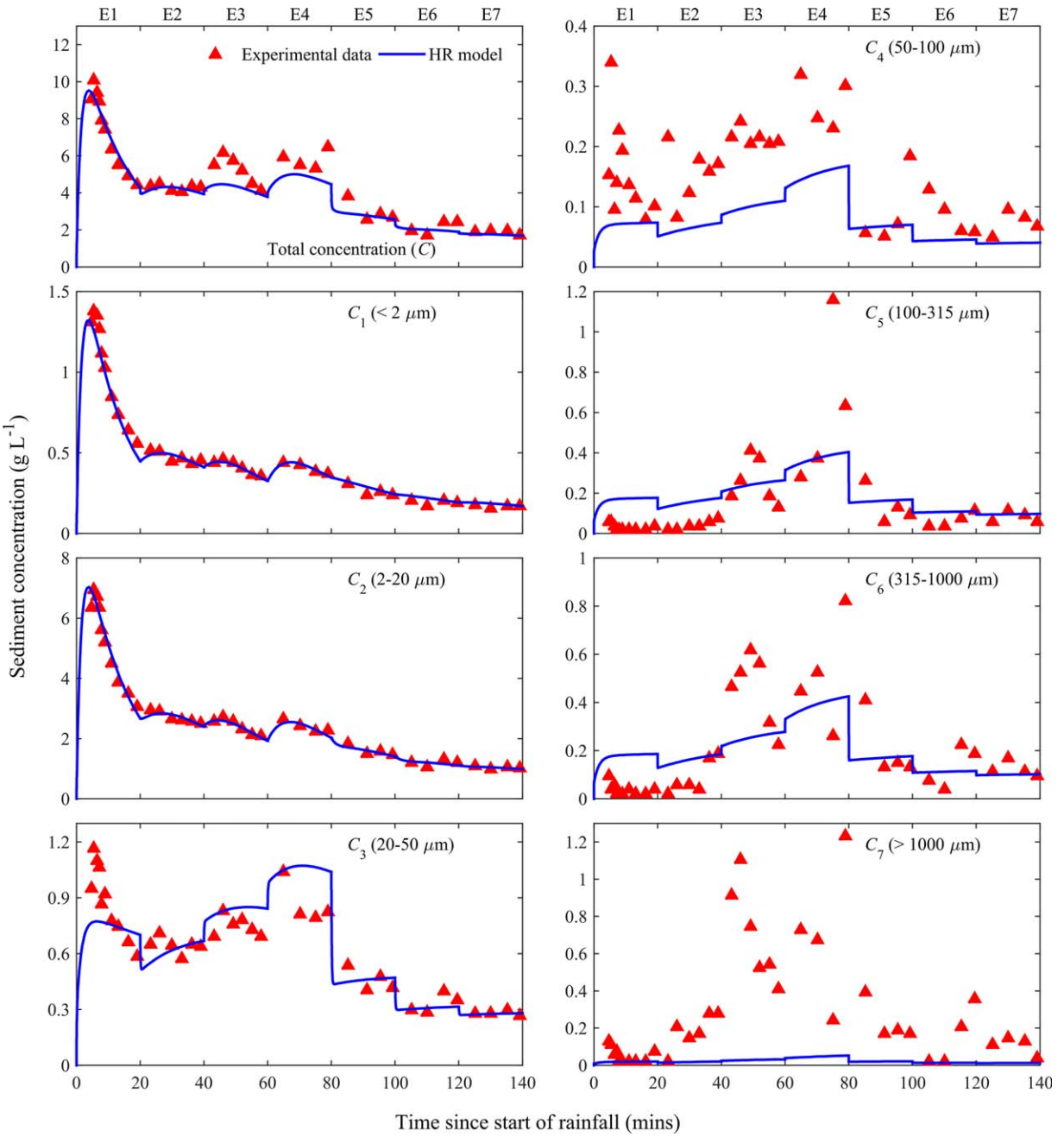


Figure 5. Total sediment concentration (C) and concentrations of the seven different particle size classes (C_1–C_7) for Collector 2. The HR model predicts the concentrations of the finer particle size classes satisfactorily. As the particles become larger, the difference between the model predictions and experimental data increases.

by the larger size classes, less erosion takes place during the falling limb of discharge in comparison to the rising limb [*Colby*, 1963; *Miller and Baharuddin*, 1987; *Sander et al.*, 2011; *Kim and Ivanov*, 2014].

Clockwise hysteresis loops were measured for the three finest particle size classes (C_1–C_3, Figures 6 and 7). However, as the sediment particles become larger (C_4–C_7), the hysteresis loops gradually become narrower and there is almost a linear relation between the discharge and sediment concentration, i.e., the hysteresis disappears. The concentration-discharge data show that, within a temporally varying rainfall event, different particle sizes not only have different hysteresis patterns, but also that their individual behaviors are strongly coupled. This is because the hysteresis patterns for the fine particles arise due to the presence of the larger particles within the original soil, which have a greater deposition rate compared to the finer particles. The

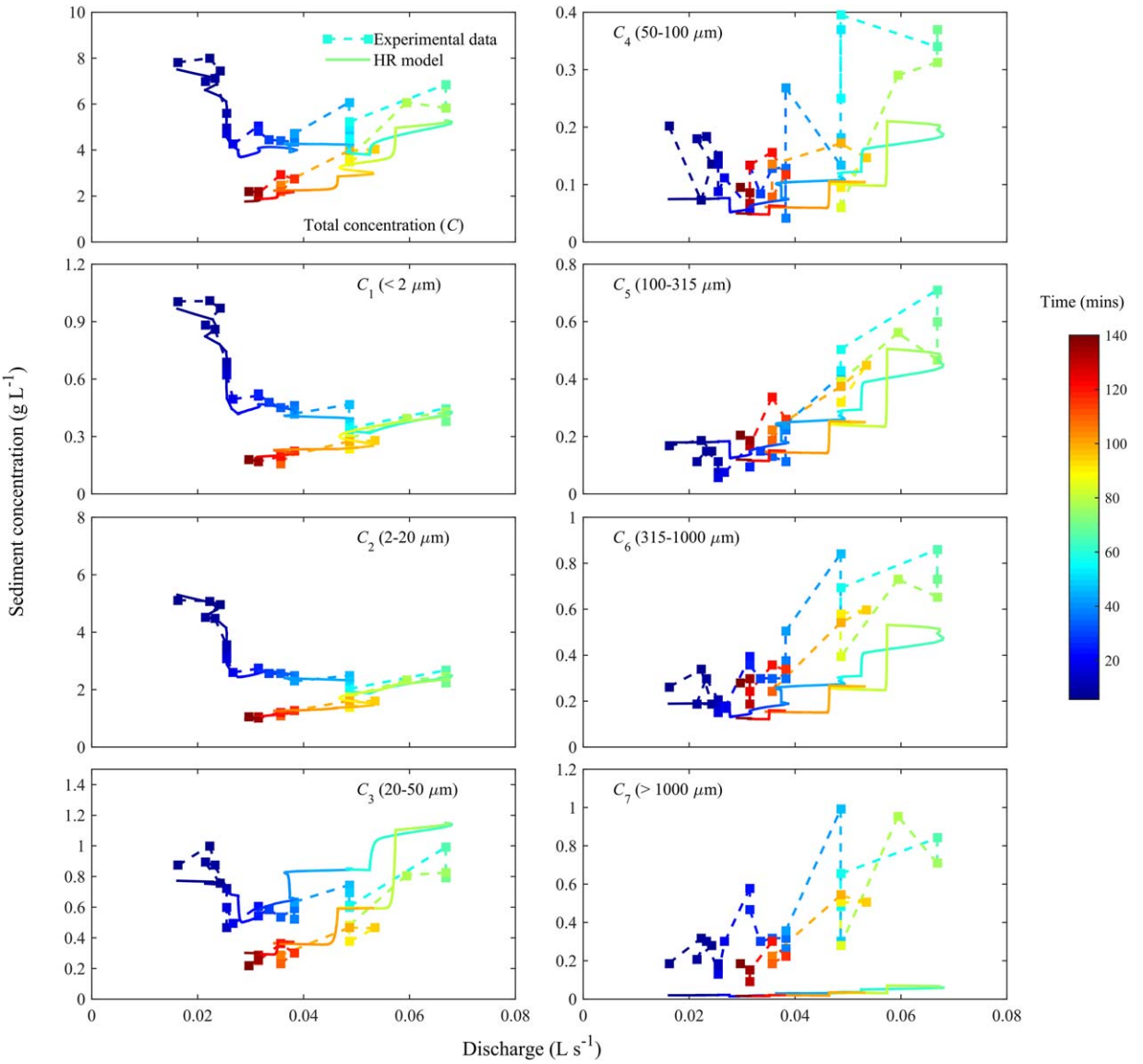


Figure 6. Hysteresis loops (measured data and HR model results) associated with the total sediment concentration (C) and individual particle size classes (C_1–C_7) (Collector 1). The elapsed time (0–140 min) is shown by the color bar.

larger particles with their nonhysteretic behavior limit the supply of the finer particles, resulting in hysteretic loops for these latter sediment sizes [*Sander et al*., 2011].

The ploughed and smoothed flume surface initially provide a source of easily erodible sediment that has a greater availability of fine particles. During the first rainfall event, rapid increases in both C_1 and C_2 occur, with $C_2 > C_1$ as the mass proportion of sediment in class 2 is far greater than that in size class 1 ($p_2 \gg p_1$, Table 1). Since the deposition rate of suspended sediment is given by $v_i C_i$, in equation (2), the smaller classes contribute minimally to the deposited layer due to their low settling velocities. As the main source of the fine particles is the original soil, access to these particles becomes reduced by growth of the deposited layer (i.e., supply limited) [*Parlange et al*., 1999; *Bussi et al*., 2014]. Therefore, both C_1 and C_2 rapidly reduce from their initial peaks. Over successive events, the deposited layer becomes increasingly dominated by larger particles with any previously deposited fine material being slowly stripped out (Figure 8).

The availability of the finer particles reduces due to different factors. First, raindrops nonpreferentially eject sediment from the bed [*Legout et al*., 2005]. Suspended transport of finer sediment sizes, however, occurs

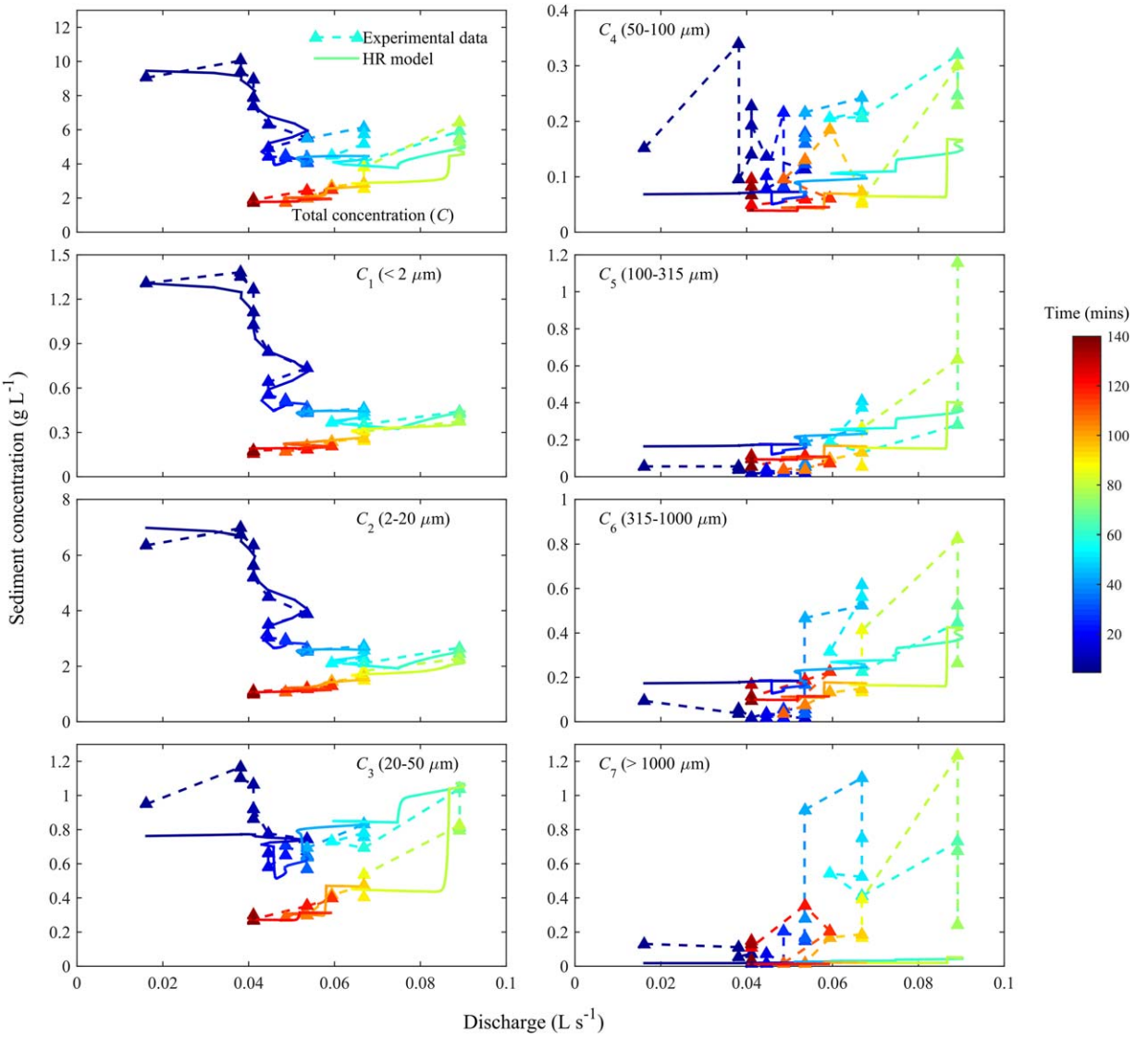


Figure 7. Hysteresis loops (measured data and HR model results) associated with the total sediment concentration (C) and individual particle size classes (C_1–C_7) (Collector 2). The elapsed time (0–140 min) is shown by the color bar.

preferentially, as does deposition of larger sediment sizes. The combination of these two effects leads to a surface soil layer that is progressively denuded of finer sediments as they are transported from the flume. Other things being equal, this means that the sediment concentrations for finer size classes leaving the flume will be reduced. Second, soil compaction decreases the depth of the soil into which the raindrops penetrate, i.e., less soil is able to be detached by the raindrop impact. Consequently, during the falling limb of the hydrograph for the same discharge, lower sediment concentrations are observed since it is now the larger, deposited particles that are being eroded. That the larger particles are seen to have similar concentrations on both the rising and falling limbs are due to their consistent availability (Figure 9) in the deposited layer. For this situation, changes in concentration between events are related to the rainfall intensity, i.e., detachment limited. Thus, the different behavior across the size classes highlights the importance of the particle size distribution in the development of hysteresis loops. These results reinforce the findings of *Bussi et al*. [2014] for the Goodwin Creek catchment and the numerical study of *Kim and Ivanov* [2014] on the role of initial loose sediment (equivalent to the deposited layer in the HR model) in determining sediment transport patterns. That is, the initial spatial distribution and sediment size class composition of the deposited layer play an important role in determining the different types and orientations of sediment hysteresis loops [*Sander et al*., 2011; *Zhong*, 2013; *Bussi et al*., 2014].

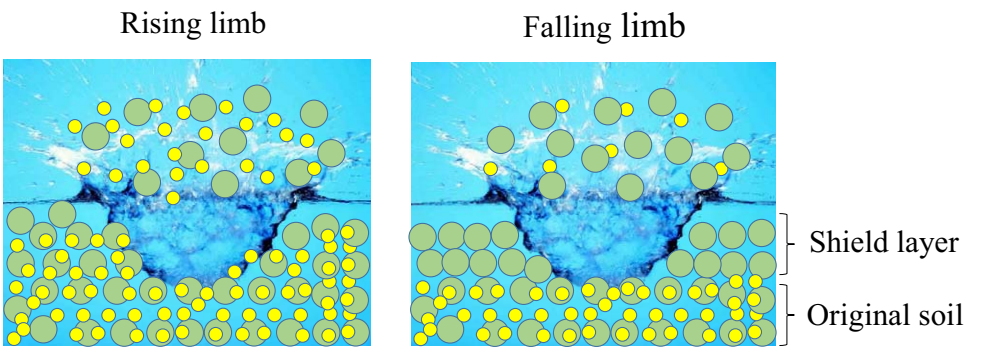


Figure 8. Schematic depiction of raindrop impact on the soil surface. Finer particles are available for suspension due to raindrop impact on the rising limb. Over time, the finer particles are preferentially removed, leaving a shield layer composed mainly of larger particle sizes [*Colby*, 1963].

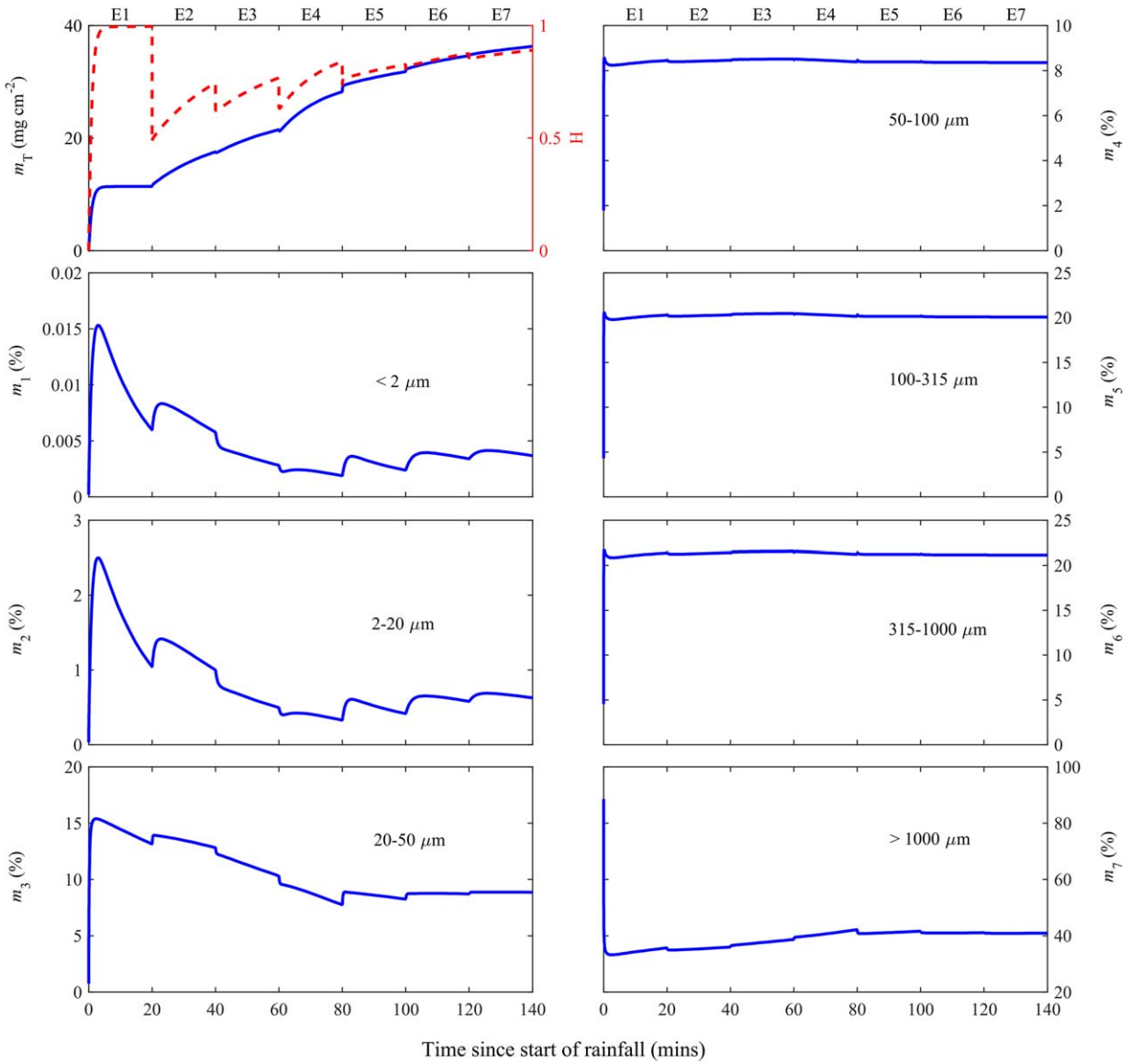


Figure 9. HR model predictions of the total mass of the deposited layer (m) and the contribution of seven different particle size classes (m_1–m_7) within the shield layer (Collector 1). The variation of degree of shielding (H) is shown along with the total mass.

Hysteresis in total sediment concentration-discharge plots for river flow was analyzed by *Williams* [1989], who explained clockwise loops as being due to either "a depletion of available sediment before water discharge has peaked" or to "the formation of an armored layer prior to the occurrence of the discharge peak." The results presented here on the sediment size classes composing the soil highlight the important role of the reduction of fines within the surface soil layer—this reduction over the course of the experiment underpins the observed hysteresis. At the same time, the surface layer protects the underlying soil, so in that sense it is an "armored layer," i.e., both reasons given by *Williams* [1989] apply to our experiments.

3.2. Model

3.2.1. Calibrated Parameters

We return to the optimized parameters for the HR model given in Table 2. The results show that the maximum detachability (a) occurs in the first rainfall event (E1). This value reduces during E2, and then varies little. Likewise, the value of critical mass (m^*) is a minimum for the first rainfall event, varying little thereafter. These results reflect the differences in the soil structure (i.e., soil compaction) that had a significant effect during the first rainfall event, but was negligible for later events.

Another factor is the water layer depth (D) that protects the soil from raindrop splash erosion (equation (3)). The modeled water depths reported in Table 2 increase as expected with rainfall intensity, but also because soil compaction during the falling limb decreases the infiltration rate and smooth the soil surface [*Jomaa et al*., 2013], D tends to be lower on the falling limb of the hydrograph for the same rainfall intensity event.

The mass of deposited sediment required for complete shielding (m^*) depends on both the rainfall rate and flow depth. For the same rainfall rate and soil condition but for a lower water depth, raindrops are able to penetrate a greater distance into the soil surface [*Hairsine et al*., 1999; *Jomaa et al*., 2012a]. Hence, a greater thickness, or increased mass m^*, is required for the deposited layer to absorb the raindrop energy and fully protect the underlying soil. Consistent with this observation, the results of Table 2 also show that, at different rainfall rates, higher values of m^* are predicted for Collector 2 on which the water layer (D) is less than for Collector 1.

The match of the model with the experimental results is good for the total sediment concentration and for the finer particle size classes, with poorer matches for the larger particles (Figures 4–7). For the largest particle size class (C_7), although the trend of the model is correct (i.e., rising and falling sediment concentrations depending on the precipitation rate), the modeled concentrations of the large particles are less than measured in the experiment. As noted previously [*Jomaa et al*., 2012b, 2013] in the model, the larger particles are assumed to be transported as suspended load that is rapidly deposited due to their high settling velocities. However, large particles are more likely transported due to rolling, saltation and ejection during the experiment, which would account for the higher measured values compared to the model predictions. A caveat on the HR model application is that, although the results are consistent with the experimental data, the model was not used to predict the experimental measurements, rather the model was calibrated to them. Our purpose here was not prediction, but to test whether the HR model could reproduce the time-dependent size class hysteretic behavior observed in the experimental results in a physically consistent manner.

3.2.2. Deposited Layer Mass

The total mass of the shield layer and its sediment-size composition is given by the calibrated HR model. In Figure 9, model results for the total mass of the deposited layer (m) and the proportion of seven particle size classes (m_1–m_7) are presented for Collector 1 only as results for Collector 2 are similar. At the start of the first rainfall event, the initially ploughed and smoothed surface easily erodes, resulting in a rapid increase in the suspended concentration (Figure 4), which is immediately followed by deposition and a rapid increase of the deposited layer (Figure 9). Initially, the deposited layer contains the smaller sediment size classes (C_1, C_2, and C_3) even though they have relatively low settling velocities. This is because the deposition rate (as given by $d_i = v_i C_i$ in equations (2) and (3)) shows that a high suspended sediment concentration can compensate for a low settling velocity to still give significant deposition of small particles. However, as time increases, the supply of the smaller particles (C_1–C_3) reduces as the original soil becomes protected, and the smaller particles within the deposited layer are gradually redetached and advected downstream to the flume exit, resulting in the increased contribution of all larger sized particles, i.e., sizes C_4 through C_7

(Figure 9) [*Heilig et al*., 2001; *Salant et al*., 2008; *Tromp-van Meerveld et al*., 2008; *Sander et al*., 2011; *Kim and Ivanov*, 2014].

The increased rainfall at the start of the second event (E2) resulted in little change in the flow depth (Table 2). At the same time, the sediment detachment rate increased, resulting in an increased value of m^* to protect the original soil and a corresponding sudden decrease in H (equation (3)). Thus, the increased rainfall rate results in increased penetration of raindrops through the depositing layer to access a greater amount of fine particles. For m_1–m_3 (Figures 8 and 9), this increase reflects the behavior seen at the beginning of the first event, but at a lower magnitude due to raindrop compaction of the soil. Simultaneously, there are small increases in the measured sediment concentrations in the effluent for size classes C_1–C_3 (Figures 4 and 5). Again, there is a rise in the contributions of the larger particles (m_4–m_7) to the deposited layer (Figure 9, E2). From event E3 onward, there is a continual removal of the small size (m_1–m_3) classes that is accompanied by growth in the contribution of the largest size class, while that of classes m_4, m_5, and m_6 remain relatively static. By this time, the deposited layer has become so dominated by the largest size classes that changes in rainfall rate (Figure 2) and flow rate (Figure 3) have only a minor impact on it.

4. Concluding Remarks

Sediment transport as a result of multiple continual rainfall events was studied via experiments and modeling. Specifically, we investigated the hysteresis loop patterns of different sediment size classes versus flume discharge for time-varying precipitation rates. To this end, seven consecutive rainfall events were applied to an initially ploughed and smoothed soil. Sediment concentrations at the flume exit were taken from samples from two collectors. The results were further analyzed by calibrating the HR model to the measurements. We examined the behavior of the different particle size classes during the multiple rainfall events in the absence of rills.

For an initially dry and ploughed soil, clockwise hysteresis loops in sediment concentration versus discharge rate were generated for the total sediment concentration and the concentrations of the finest particle size classes. In contrast, for the larger particle sizes, the hysteresis loops are narrower and have a more irregular shape. Indeed, it is not clear whether they exhibit hysteresis. The results suggest that the contribution of the finer particles to the total eroded mass reduces over the course of the experiment, independent of the precipitation rate (source-limited delivery). However, the contribution of larger particles to the total eroded mass increased during the rising limb and decreased during the falling limb, reflecting transport-limited behavior of the larger size classes. We remark that soil compaction is not necessary for the appearance of hysteresis. Instead, at least for our experiments, the key factor is the decreasing availability of finer sediments. The combination of deposited material and compaction also protects the original soil from raindrop erosion. Another factor affecting raindrop erosion is surface water, since increasing water depths protect the soil. The average surface water depth changes due to compaction and the variable precipitation rate. Consistent with the low precipitation rates applied during most of the experiment, modeled water depths were small according to the calibrated HR model (Table 2), and which we noted visually. Consequently, it is unlikely that water depth played a significant role protecting the soil in the results reported here.

A crucial feature of the HR model is its ability to simulate the sediment size distribution in the deposited layer (i.e., deposition of previously eroded sediment), which provides a quantitative basis for simulating hysteresis in the discharge-sediment concentration plots. The model results show that the reduction in the availability of the finer sediment sizes in the deposited layer results in hysteresis in the total sediment concentration plots, as well as in the finer size classes. Additionally, the model results are consistent with the reduction (even absence) of hysteresis evident in the experimental data for the larger sediment size classes.

However, the just-mentioned reduction of the proportion of fine sediment sizes is not essential for hysteresis to occur. To be clear, the distribution of size classes plays an important role in determining the shape and magnitude of the hysteresis loop, but it is not the controlling factor. In the extreme case of a soil that is composed of only a single size class, simulations with the HR model show that clockwise, anticlockwise, and figure eight loops can still be obtained. As found by *Sander et al*. [2011], the shapes of the hysteresis loops produced are still dependent on the initial condition of the deposited layer, i.e., on the initial availability of easily erodible sediment. These shapes are dependent on particle size. That is, as the (single) particle size

increases, the size of the loop diminishes, and hysteresis effectively ceases, in agreement with the behavior of the largest size classes shown in Figures 6 and 7.

Acknowledgments
Financial support was provided by the Swiss National Science Foundation (200021_144320). Pierre-Alain Hildenbrand, Jacques Roland Golay, and Htet Kyi Wynn provided essential technical support for the execution of the experiment. The code and experimental data will be made available upon request to Ecological Engineering Laboratory (ECOL), http://ecol.epfl.ch/.

References

Aich, V., A. Zimmermann, and H. Elsenbeer (2014), Quantification and interpretation of suspended-sediment discharge hysteresis patterns: How much data do we need?, *Catena*, *122*, 120–129, doi:10.1016/j.catena.2014.06.020.

Alemayehu, W., E. Teklu, and D. Prhaba (2014), Sediment and nutrient lost by runoff from two watersheds, Digga district in Blue Nile basin, Ethiopia, *Afr. J. Environ. Sci. Technol.*, *8*(9), 498–510, doi:10.5897/AJEST2014.1747.

Arjmand Sajjadi, S., and M. Mahmoodabadi (2015), Sediment concentration and hydraulic characteristics of rain-induced overland flows in arid land soils, *J. Soils Sediments*, *15*(3), 710–721, doi:10.1007/s11368-015-1072-z.

Baril, P. (1991), Erodibilité des sols et érodabilité des terres: Application au plateau vaudois, PhD thesis, Ecole Polytech. Féd. de Lausanne (EPFL), Lausanne, Switzerland, doi:10.5075/epfl-thesis-940.

Barry, D. A., G. C. Sander, S. Jomaa, B. C. P. Heng, J.-Y. Parlange, I. G. Lisle, and W. L. Hogarth (2010), Exact solutions of the Hairsine-Rose precipitation-driven erosion model for a uniform grain-sized soil, *J. Hydrol.*, *389*(3–4), 399–405, doi:10.1016/j.jhydrol.2010.06.016.

Batalla, R. J., C. M. Gómez, and G. M. Kondolf (2004), Reservoir-induced hydrological changes in the Ebro River basin (NE Spain), *J. Hydrol.*, *290*(1–2), 117–136, doi:10.1016/j.jhydrol.2003.12.002.

Beuselinck, L., G. Govers, P. B. Hairsine, G. C. Sander, and M. Breynaert (2002), The influence of rainfall on sediment transport by overland flow over areas of net deposition, *J. Hydrol.*, *257*(1–4), 145–163, doi:10.1016/S0022-1694(01)00548-0.

Buendia, C., D. Vericat, R. J. Batalla, and C. N. Gibbins (2015), Temporal dynamics of sediment transport and transient in-channel storage in a highly erodible catchment, *Land Degrad. Develop.*, *27*(4), 1045–1063, doi:10.1002/ldr.2348.

Bussi, G., F. Francés, J. J. Montoya, and P. Y. Julien (2014), Distributed sediment yield modelling: Importance of initial sediment conditions, *Environ. Model. Software*, *58*, 58–70, doi:10.1016/j.envsoft.2014.04.010.

Cerdà, A. (2001), Effects of rock fragment cover on soil infiltration, interrill runoff and erosion, *Eur. J. Soil Sci.*, *52*(1), 59–68, doi:10.1046/j.1365-2389.2001.00354.x.

Cerdà, A., A. G. Morera, and M. B. Bodí (2009), Soil and water losses from new citrus orchards growing on sloped soils in the western Mediterranean basin, *Earth Surf. Processes Landforms*, *34*(13), 1822–1830, doi:10.1002/esp.1889.

Colby, B. R. (1963), Fluvial sediments: a summary of source, transportation, deposition, and measurement of sediment discharge (No. 1181), US Government Printing Office, Washington. [Available at https://pubs.usgs.gov/bul/1181a/report.pdf.]

Dai, Z., S. Fagherazzi, X. Mei, and J. Gao (2016), Decline in suspended sediment concentration delivered by the Changjiang (Yangtze) River into the East China Sea between 1956 and 2013, *Geomorphology*, *268*, 123–132, doi:10.1016/j.geomorph.2016.06.009.

Dean, D. J., D. J. Topping, J. C. Schmidt, R. E. Griffiths, and T. A. Sabol (2016), Sediment supply versus local hydraulic controls on sediment transport and storage in a river with large sediment loads, *J. Geophys. Res.*, *121*, 82–110, doi:10.1002/2015JF003436.

De Girolamo, A. M. M., G. Pappagallo, and A. Lo Porto (2015), Temporal variability of suspended sediment transport and rating curves in a Mediterranean river basin: The Celone (SE Italy), *Catena*, *128*, 135–143, doi:10.1016/j.catena.2014.09.020.

Eder, A., P. Strauss, T. Krueger, and J. N. Quinton (2010), Comparative calculation of suspended sediment loads with respect to hysteresis effects (in the Petzenkirchen catchment, Austria), *J. Hydrol.*, *389*(1–2), 168–176, doi:10.1016/j.jhydrol.2010.05.043.

Gao, B., M. T. Walter, T. S. Steenhuis, J.-Y. Parlange, K. Nakano, C. W. Rose, and W. L. Hogarth (2003), Investigating ponding depth and soil detachability for a mechanistic erosion model using a simple experiment, *J. Hydrol.*, *277*(1–2), 116–124, doi:10.1016/S0022-1694(03)00085-4.

Gao, P., and M. Josefson (2012), Event-based suspended sediment dynamics in a central New York watershed, *Geomorphology*, *139 140–*, 425–437, doi:10.1016/j.geomorph.2011.11.007.

Ghahramani, A., and Y. Ishikawa (2013), Water flux and sediment transport within a forested landscape: The role of connectivity, subsurface flow, and slope length scale on transport mechanism, *Hydrol. Processes*, *27*(26), 4091–4102, doi:10.1002/hyp.9791.

Ghahramani, A., I. Yoshiharu, and S. M. Mudd (2012), Field experiments constraining the probability distribution of particle travel distances during natural rainstorms on different slope gradients, *Earth Surf. Processes Landforms*, *37*(5), 473–485, doi:10.1002/esp.2253.

Hairsine, P. B., and C. W. Rose (1991), Rainfall detachment and deposition: Sediment transport in the absence of flow-driven processes, *Soil Sci. Soc. Am. J.*, *55*(2), 320, doi:10.2136/sssaj1991.03615995005500020003x.

Hairsine, P. B., and C. W. Rose (1992), Modeling water erosion due to overland flow using physical principles: 1. Sheet flow, *Water Resour. Res.*, *28*(1), 237–243, doi:10.1029/91WR02380.

Hairsine, P. B., G. C. Sander, C. W. Rose, J.-Y. Parlange, W. L. Hogarth, I. Lisle, and H. Rouhipour (1999), Unsteady soil erosion due to rainfall impact: A model of sediment sorting on the hillslope, *J. Hydrol.*, *220*(3–4), 115–128, doi:10.1016/S0022-1694(99)00068-2.

Halliday, S. J., R. A. Skeffington, M. J. Bowes, E. Gozzard, J. R. Newman, M. Loewenthal, E. J. Palmer-Felgate, H. P. Jarvie, and A. J. Wade (2014), The water quality of the River Enborne, UK: Observations from high-frequency monitoring in a rural, lowland river system, *Water*, *6*(1), 150–180, doi:10.3390/w6010150.

Heilig, A., D. DeBruyn, M. T. Walter, C. W. Rose, J.-Y. Parlange, T. S. Steenhuis, G. C. Sander, P. B. Hairsine, W. L. Hogarth, and L. P. Walker (2001), Testing a mechanistic soil erosion model with a simple experiment, *J. Hydrol.*, *244*(1–2), 9–16, doi:10.1016/S0022-1694(00)00400-5.

Heng, B. C. P., G. C. Sander, and C. F. Scott (2009), Modeling overland flow and soil erosion on nonuniform hillslopes: A finite volume scheme, *Water Resour. Res.*, *45*, W05423, doi:10.1029/2008WR007502.

Heng, B. C. P., G. C. Sander, A. Armstrong, J. N. Quinton, J. H. Chandler, and C. F. Scott (2011), Modeling the dynamics of soil erosion and size-selective sediment transport over nonuniform topography in flume-scale experiments, *Water Resour. Res.*, *47*, W02513, doi:10.1029/2010WR009375.

Jomaa, S., D. A. Barry, A. Brovelli, G. C. Sander, J.-Y. Parlange, B. C. P. Heng, and H. J. Tromp-van Meerveld (2010), Effect of raindrop splash and transversal width on soil erosion: Laboratory flume experiments and analysis with the Hairsine-Rose model, *J. Hydrol.*, *395*(1–2), 117–132, doi:10.1016/j.jhydrol.2010.10.021.

Jomaa, S., D. A. Barry, B. C. P. Heng, A. Brovelli, G. C. Sander, and J.-Y. Parlange (2012a), Influence of rock fragment coverage on soil erosion and hydrological response: Laboratory flume experiments and modeling, *Water Resour. Res.*, *48*, W05535, doi:10.1029/2011WR011255.

Jomaa, S., D. A. Barry, A. Brovelli, B. C. P. Heng, G. C. Sander, J.-Y. Parlange, and C. W. Rose (2012b), Rain splash soil erosion estimation in the presence of rock fragments, *Catena*, *92*, 38–48, doi:10.1016/j.catena.2011.11.008.

Jomaa, S., D. A. Barry, B. C. P. Heng, A. Brovelli, G. C. Sander, and J.-Y. Parlange (2013), Effect of antecedent conditions and fixed rock fragment coverage on soil erosion dynamics through multiple rainfall events, *J. Hydrol.*, *484*, 115–127, doi:10.1016/j.jhydrol.2013.01.021.

Karimaee Tabarestani, M., and A. R. Zarrati (2014), Sediment transport during flood event: A review, *Int. J. Environ. Sci. Technol.*, *12*(2), 775–788, doi:10.1007/s13762-014-0689-6.
Keesstra, S. D., J. Maroulis, E. Argaman, A. Voogt, and L. Wittenberg (2014), Effects of controlled fire on hydrology and erosion under simulated rainfall, *Cuad. Invest. Geogr.*, *40*(2), 269–293, doi:10.18172/cig.2532.
Kennedy, J. (2010), Particle swarm optimization, *Encycl. Mach. Learn.*, *46*(11), 685–691, doi:10.1109/ICNN.1995.488968.
Kim, J., and V. Y. Ivanov (2014), On the nonuniqueness of sediment yield at the catchment scale: The effects of soil antecedent conditions and surface shield, *Water Resour. Res.*, *50*, 1025–1045, doi:10.1002/2013WR014580.
Kim, J., V. Y. Ivanov, and N. D. Katopodes (2013), Modeling erosion and sedimentation coupled with hydrological and overland flow processes at the watershed scale, *Water Resour. Res.*, *49*, 5134–5154, doi:10.1002/wrcr.20373.
Kim, J., V. Y. Ivanov, and S. Fatichi (2016a), Environmental stochasticity controls soil erosion variability, *Sci. Rep.*, *6*, 22,065, doi:10.1038/srep22065.
Kim, J., M. C. Dwelle, S. K. Kampf, S. Fatichi, and V. Y. Ivanov (2016b), On the non-uniqueness of the hydro-geomorphic responses in a zero-order catchment with respect to soil moisture, *Adv. Water Resour.*, *92*, 73–89, doi:10.1016/j.advwatres.2016.03.019.
Kinnell, P. I. A. (2013), Modeling of the effect of flow depth on sediment discharged by rain-impacted flows from sheet and interrill erosion areas: A review, *Hydrol. Processes*, *27*(18), 2567–2578, doi:10.1002/hyp.9363.
Klein, M. (1984), Anti clockwise hysteresis in suspended sediment concentration during individual storms: Holbeck catchment; Yorkshire, England, *Catena*, *11*(2–3), 251–257, doi:10.1016/0341-8162(84)90014-6.
Legout, C., S. Leguédois, Y. Le Bissonnais, and O. Malam Issa (2005), Splash distance and size distributions for various soils, *Geoderma*, *124*(3–4), 279–292, doi:10.1016/j.geoderma.2004.05.006.
Lisle, I. G., C. W. Rose, W. L. Hogarth, P. B. Hairsine, G. C. Sander, and J.-Y. Parlange (1998), Stochastic sediment transport in soil erosion, *J. Hydrol.*, *204*(1–4), 217–230, doi:10.1016/S0022-1694(97)00123-6.
Lloyd, C. E. M., J. E. Freer, P. J. Johnes, and A. L. Collins (2016), Using hysteresis analysis of high-resolution water quality monitoring data, including uncertainty, to infer controls on nutrient and sediment transfer in catchments, *Sci. Total Environ.*, *543*(2016), 388–404, doi:10.1016/j.scitotenv.2015.11.028.
Marchamalo, M., J. M. Hooke, and P. J. Sandercock (2015), Flow and sediment connectivity in semi-arid landscapes in SE Spain: Patterns and controls, *Land Degrad. Develop.*, *27*(4), 1032–1044, doi:10.1002/ldr.2352.
Masselink, R. J. H., S. D. Keesstra, A. J. A. M. Temme, M. Seeger, R. Giménez, and J. Casalí (2016), Modelling discharge and sediment yield at catchment scale using connectivity components, *Land Degrad. Develop.*, *27*(4), 933–945, doi:10.1002/ldr.2512.
Miller, W. P., and M. K. Baharuddin (1987), Particle size of interrill-eroded sediments from highly weathered soils, *Soil Sci. Soc. Am. J.*, *51*(6), 1610, doi:10.2136/sssaj1987.03615995005100060037x.
Nadal-Romero, E., D. Regüés, and J. Latron (2008), Relationships among rainfall, runoff, and suspended sediment in a small catchment with badlands, *Catena*, *74*(2), 127–136, doi:10.1016/j.catena.2008.03.014.
O'Connell, S., and A. Siafarikas (2010), Addison disease: Diagnosis and initial management, *Aust. Fam. Phys.*, *39*(11), 834–837, doi:10.1024/0301-1526.32.1.54.
Oeurng, C., S. Sauvage, and J.-M. Sánchez-Pérez (2011), Assessment of hydrology, sediment and particulate organic carbon yield in a large agricultural catchment using the SWAT model, *J. Hydrol.*, *401*(3–4), 145–153, doi:10.1016/j.jhydrol.2011.02.017.
Parlange, J.-Y., W. L. Hogarth, C. W. Rose, G. C. Sander, P. B. Hairsine, and I. Lisle (1999), Addendum to unsteady soil erosion model, *J. Hydrol.*, *217*(1–2), 149–156, doi:10.1016/S0022-1694(99)00012-8.
Pietroń, J., J. Jarsjö, A. O. Romanchenko, and S. R. Chalov (2015), Model analyses of the contribution of in-channel processes to sediment concentration hysteresis loops, *J. Hydrol.*, *527*, 576–589, doi:10.1016/j.jhydrol.2015.05.009.
Polyakov, V. O., and M. A. Nearing (2003), Sediment transport in rill flow under deposition and detachment conditions, *Catena*, *51*(1), 33–43, doi:10.1016/S0341-8162(02)00090-5.
Prosdocimi, M., A. Cerdà, and P. Tarolli (2016), Soil water erosion on Mediterranean vineyards: A review, *Catena*, *141*, 1–21, doi:10.1016/j.catena.2016.02.010.
Rodrigo Comino, J., et al. (2016), Quantitative comparison of initial soil erosion processes and runoff generation in Spanish and German vineyards, *Sci. Total Environ.*, *565*, 1165–1174, doi:10.1016/j.scitotenv.2016.05.163.
Rossi, L., N. Chèvre, R. Fankhauser, J. Margot, R. Curdy, M. Babut, and D. A. Barry (2013), Sediment contamination assessment in urban areas based on total suspended solids, *Water Res.*, *47*(1), 339–350, doi:10.1016/j.watres.2012.10.011.
Sadeghi, S. H. R., T. Mizuyama, S. Miyata, T. Gomi, K. Kosugi, T. Fukushima, S. Mizugaki, and Y. Onda (2008), Determinant factors of sediment graphs and rating loops in a reforested watershed, *J. Hydrol.*, *356*(3–4), 271–282, doi:10.1016/j.jhydrol.2008.04.005.
Salant, N. L., M. A. Hassan, and C. V. Alonso (2008), Suspended sediment dynamics at high and low storm flows in two small watersheds, *Hydrol. Processes*, *22*(11), 1573–1587, doi:10.1002/hyp.6743.
Sander, G. C., P. B. Hairsine, C. W. Rose, D. Cassidy, J.-Y. Parlange, W. L. Hogarth, and I. G. Lisle (1996), Unsteady soil erosion model, analytical solutions and comparison with experimental results, *J. Hydrol.*, *178*(1–4), 351–367, doi:10.1016/0022-1694(95)02810-2.
Sander, G. C., J.-Y. Parlange, D. A. Barry, M. B. Parlange, and W. L. Hogarth (2007), Limitation of the transport capacity approach in sediment transport modeling, *Water Resour. Res.*, *43*, W02403, doi:10.1029/2006WR005177.
Sander, G. C., T. Zheng, P. Heng, Y. Zhong, and D. A. Barry (2011), Sustainable soil and water resources: Modelling soil erosion and its impact on the environment, in *19th International Congress on Modelling and Simulation*, pp. 45–56, Model. and Simul. Soc. of Aust. and N. Z. Inc., Perth, Australia. [Available at http://mssanz.org.au/modsim2011/plenary.htm.]
Seeger, M., M.-P. Errea, S. Beguería, J. Arnáez, C. Martí, and J. García-Ruiz (2004), Catchment soil moisture and rainfall characteristics as determinant factors for discharge/suspended sediment hysteretic loops in a small headwater catchment in the Spanish pyrenees, *J. Hydrol.*, *288*(3–4), 299–311, doi:10.1016/j.jhydrol.2003.10.012.
Sherriff, S. C., J. S. Rowan, O. Fenton, P. Jordan, A. R. Melland, P. E. Mellander, and D. Huallacháin (2016), Storm event suspended sediment-discharge hysteresis and controls in agricultural watersheds: Implications for watershed scale sediment management, *Environ. Sci. Technol.*, *50*(4), 1769–1778, doi:10.1021/acs.est.5b04573.
Smith, H. G., and D. Dragovich (2009), Interpreting sediment delivery processes using suspended sediment-discharge hysteresis patterns from nested upland catchments, south-eastern Australia, *Hydrol. Processes*, *23*(17), 2415–2426, doi:10.1002/hyp.7357.
Stokes, G. G. (1850), On the effect of the internal friction of fluids on the motion of pendulums, in *Transactions of the Cambridge Philosophical Society*, vol. 9, p. 8, Cambridge Univ. Press, Cambridge, U. K.
Strohmeier, S., G. Laaha, H. Holzmann, and A. Klik (2016), Magnitude and occurrence probability of soil loss: A risk analytical approach for the plot scale for two sites in lower Austria, *Land Degrad. Develop.*, *27*(1), 43–51, doi:10.1002/ldr.2354.
Sun, L., M. Yan, Q. Cai, and H. Fang (2016), Suspended sediment dynamics at different time scales in the Loushui River, south-central China, *Catena*, *136*, 152–161, doi:10.1016/j.catena.2015.02.014.

Tromp-van Meerveld, H. J., J.-Y. Parlange, D. A. Barry, M. F. Tromp, G. C. Sander, M. T. Walter, and M. B. Parlange (2008), Influence of sediment settling velocity on mechanistic soil erosion modeling, *Water Resour. Res.*, *44*, W06401, doi:10.1029/2007WR006361.

Van Oost, K., L. Beuselinck, P. B. Hairsine, and G. Govers (2004), Spatial evaluation of a multi-class sediment transport and deposition model, *Earth Surf. Processes Landforms*, *29*(8), 1027–1044, doi:10.1002/esp.1089.

Viani, J.-P. (1986), Contribution à l'étude expérimentale de l'érosion hydrique, PhD thesis, Ecole Polytech. Féd. de Lausanne (EPFL), Lausanne, Switzerland, doi:10.5075/epfl-thesis-641.

Walling, D. E., and B. W. Webb (1985), Estimating the discharge of contaminants to coastal waters by rivers: Some cautionary comments, *Mar. Pollut. Bull.*, *16*(12), 488–492, doi:10.1016/0025-326X(85)90382-0.

Williams, G. P. (1989), Sediment concentration versus water discharge during single hydrologic events in rivers, *J. Hydrol.*, *111*(1–4), 89–106, doi:10.1016/0022-1694(89)90254-0.

Wood, P. J., and P. D. Armitage (1997), Biological effects of fine sediment in the lotic environment, *Environ. Manage. N. Y.*, *21*(2), 203–217, doi:10.1007/s002679900019.

Yeshaneh, E., A. Eder, and G. Blöschl (2014), Temporal variation of suspended sediment transport in the Koga catchment, North Western Ethiopia and environmental implications, *Hydrol. Processes*, *28*(24), 5972–5984, doi:10.1002/hyp.10090.

Zhong, Y. (2013), Modelling sediment transportation and overland flow, PhD thesis, Univ. of Oxford, Oxford, U. K. [Available at https://ora.ox.ac.uk:443/objects/uuid:a45eefae-5a0f-4917-9abb-261ae792f2ee.]